Frontiers of Physics
https://doi.org/10.1007/s11467-019-0907-2
Front. Phys.
14(4), 43403 (2019)

REVIEW ARTICLE

Dephasing effects in topological insulators

Junjie Qi[1,2], **Haiwen Liu**[3], **Hua Jiang**[4,5], **X. C. Xie**[1,2,†]

[1] *International Center for Quantum Materials and School of Physics, Peking University, Beijing 100871, China*
[2] *Collaborative Innovation Center of Quantum Matter, Beijing, China*
[3] *Center for Advanced Quantum Studies, Department of Physics, Beijing Normal University, Beijing 100875, China*
[4] *School of Physical Science and Technology, Soochow University, Suzhou 215006, China*
[5] *Institute for Advanced Study, Soochow University, Suzhou 215006, China*
Corresponding author. E-mail: †*xcxie@pku.edu.cn*
Received March 29, 2019; accepted May 16, 2019

Topological insulators, a class of typical topological materials in both two dimensions and three dimensions, are insulating in bulk and metallic at surface. The spin-momentum locked surface states and peculiar transport properties exhibit promising potential applications on quantum devices, which generate extensive interest in the last decade. Dephasing is the process of the loss of phase coherence, which inevitably exists in a realistic sample. In this review, we focus on recent progress in dephasing effects on the topological insulators. In general, there are two types of dephasing processes: normal dephasing and spin dephasing. In two-dimensional topological insulators, the phenomenologically numerical investigation shows that the longitudinal resistance plateaus is robust against normal dephasing but fragile with spin dephasing. Several microscopic mechanisms of spin dephasing are then discussed. In three-dimensional topological insulators, the helical surface states exhibit a helical spin texture due to the spin-momentum locking mechanism. Thus, normal dephasing has close connection to spin dephasing in this case, and gives rise to anomalous "gap-like" feature. Dephasing effects on properties of helical surface states are investigated.

Keywords dephasing effects, topological insulators, backscattering

Contents

1 Introduction 1
2 Dephasing effects in 2D topological insulators 3
2.1 Phenomenological investigation of dephasing effects on transport properties 3
2.1.1 Longitudinal resistance behaviours 3
2.1.2 Quantized spin Hall resistance 4
2.2 Latest development of microscopic mechanisms of spin dephasing 5
2.2.1 Puddles combined with electron–phonon interaction enhanced spin dephasing mechanism 5
2.2.2 Puddles combined with electron–electron interaction enhanced spin dephasing mechanism 7
3 Dephasing effects in 3D topological insulators 7
3.1 Impurities induced dephasing effects on the helical surface states 7
3.1.1 Origin of the normal dephasing 8
3.1.2 Backscattering cross section 8
3.1.3 Anomalous "gap-like" feature 9
3.2 Puddles induced dephasing effects on the helical surface states 10
4 Conclusions and outlook 10
Acknowledgements 11
References and notes 11

*Special Topic: Recent Advances in Topological Materials (Eds. Yugui Yao, Xiangang Wan, Shengyuan A. Yang & Hua Chen).

1 Introduction

The past decade has been the rapid development of topological materials due to their novel properties and huge potential applications in quantum computing and manufacturing quantum devices. Topological materials contain a variety of confirmed members with more candidates waiting to join. The topological phases were firstly introduced aiming at explaining the properties of the quantum Hall effect (QHE) [1, 2]. The strong magnetic field in the two-dimensional (2D) electron gas can give rise to Landau-level quantization, and in high quality samples with high mobility the system exhibits the QHE [2, 3]. The most striking feature in QHE is that chiral edge states existing between Landau-levels lead to the quantized Hall conductance for a range of magnetic field, which can be understood in terms of topological invariants known as Chern or Thouless–Kohmoto–Nightingale–Nijs (TKNN) numbers [4, 5]. Due to the macroscopic separation of protected chiral edge states, the backscattering is forbidden. Thus, the Hall resistance plateaus survives in

© Higher Education Press and Springer-Verlag GmbH Germany, part of Springer Nature 2019

macroscopic systems, insensitive to disorder and dephasing effect. However, QHE requires the strong magnetic field, and unfortunately, it is almost impossible to generate such a strong magnetic field outside the laboratory. Alternatively, the quantum anomalous Hall effect (QAHE) was then proposed to harbor gapless chiral edge states with ferromagnetism. Haldane theoretically proposed a 2D honeycomb-lattice QAHE model resulting from breaking of time-reversal symmetry (TRS) without magnetic field [6]. However, since the 2D honeycomb-lattice model was not realized until 2004 and the manipulation of magnetic flux has been challenging in the condensed matter physics, the first observation of QAHE was reported in Cr-doped $(Bi, Sb)_2Te_3$ thin films in 2013 [7].

The 2D topological insulator was firstly predicted in graphene, lately known as quantum spin Hall effects (QSHE) by Kane and Mele in 2005 [8, 9]. The intrinsic spin–orbit coupling (SOC) converts graphene from an ideal semi-metallic state to a QSH one, which has metallic helical edge states protected by a bulk gap. As opposed to QHE, the electrons in QSH edge channel are spin-momentum locked. They counter-propagate with opposite spins locked perpendicular to their momentums. Thus, the QSHE can be regarded as two copies of QAHE with opposite Chern numbers, which leads to the quantized spin Hall conductance. Furthermore, TRS was found to play a key role in QSHE [9]. A topological nontrivial state described by TKNN numbers can only occur when TRS is broken, while a QSH state is found to be characterized by a topological Z_2 invariant with TRS [9]. Two counter-propagating edge states form a Kramers pair in QSHE which are immune to non-magnetic impurity backscattering, regardless of spin-rotation symmetry. Due to TRS and helical edge states, there is no Hall resistance in QSHE, whereas the longitudinal resistance exhibits the quantized plateaus. Though Kane and Mele suggested a structure to realize a QSH phase, the intrinsic SOC in graphene is extremely weak, about 8×10^{-4} meV, allows the QSHE to occur only at an unrealistical low temperature experimentally [10–14]. Fortunately, Bernevig *et al.* theoretically proposed that QSHE can be realized in zinc-blende semiconductors such as GaAs [15] and HgTe quantum wells (QWs) [16]. Soon after the theoretical proposal, the QSHE is experimentally verified in HgTe QWs [17], and then observed in InAs/GaSb heterojunctions [18]. Nowadays, there is a boom in QSHE researches by theoretical predictions [19–34], experimental realizations and characterizations [35–42] and demonstrations of exotic properties [43–45]. And of all the experimental characterizations, the quantized longitudinal resistance was regarded as the smoking gun for the QSHE. However, up to now, the quantized longitudinal resistance can only be observed in mesoscopic samples, which deviates from the quantized value in macroscopic systems [17, 38, 39].

A topological nontrivial state characterized by Chern numbers can only exist in even dimensions. By contrast, the state featured by a Z_2 topological invariant can be generalized into a 3D version, known as a topological insulator (TI). Fu *et al.* firstly predicted that alloy $Bi_{1-x}Sb_x$ would be a 3D TI [46] and is then observed [47]. A 3D TI phase has gapped bulk states and 2D helical surface states. However, the surface states in $Bi_{1-x}Sb_x$ turn out to be very complex. The tetradymite semiconductors Bi_2Te_3, Bi_2Se_3, and Sb_2Te_3 are expected to be 3D TIs [48]. Bi_2Se_3 is stoichiometric, and hence can be prepared as a sample with higher purity than an alloy $Bi_{1-x}Sb_x$. Hasan's group observed the single Dirac-cone surface state of Bi_2Se_3 samples [49, 50]. Then, a pure topological insulator phase without bulk carriers was first manifested in Bi_2Te_3 [51]. The elegant electronic structure and mature manufacturing techniques greatly promote researches on 3D TIs [52–57]. Analogy with 2D TIs, spin-momentum locked helical surface states are also the hallmark of 3D TIs. More intriguingly, the TI surface exhibits a helical spin texture which leads to the exotic transport properties and spintronics applications [49, 58]. The TRS guarantees the robustness of helical surface states against weak disorder. In common, the helical surface states are stable except the bulk gaps are closed and reopen. Besides, the topological states can be extended into other discrete symmetries [59, 60].

Dephasing is the process of carriers' phase coherence loss by definition. In a realistic sample, dephasing process is generally classified into two types: normal dephasing and spin dephasing. Normal dephasing, referring to electron–phonon interactions or electron–electron interactions, etc. [61, 62], contributes to phase relaxation but does not flip spin of electrons. Conversely, spin dephasing process affects not only phase relaxation but also spin memory. Jiang *et al.* investigated the longitudinal resistance in QSHE under two dephasing effects. By phenomenologically numerical study, they found that the quantized longitudinal plateaus is robust against normal dephasing but fragile with spin dephasing [63]. The theoretical results are in agreement with the first QSHE experiments observation that the quantized longitudinal plateaus can only be observed in mesoscopic samples [17, 38, 39]. Further transport measurements in InAs/GaSb QWs strongly confirmed that the spin dephasing is the dominant edge scattering process in this system [44]. Therefore, investigating spin dephasing effects in QSHE is a continuing concern. In addition to a single mechanism, e.g., magnetic impurities or spin fluctuation individually [64, 65], the latest developments of microscopic mechanisms of spin dephasing rely on the joint effects below: (i) electron–electron interaction and the momentum linear k-order Rashba SOC for a extended QSH state [66, 67]; (ii) the k^3-order Rashba SOC term and electron–phonon interaction for a extended QSH state [68]; (iii) k-order Rashba SOC and electron–phonon interaction for a bound QSH state [69]. Next, the dephasing effects on transport properties in 3D TIs are introduced.

The 2D spin-momentum locked surface states exhibit a chiral spin texture. Thus, it is meaningless to distinguish normal dephasing from spin dephasing for 3D TIs. Liu *et al.* found that the combination of normal dephasing and impurity scattering also leads to dramatic backscattering [70] and causes surface anomalous gap without TRS broken. Besides, Liao *et al.* showed that variable-range-hopping (VRH) mechanism in 3D TI thin films provides a new dephasing mechanism [71].

The outline of the article is as follows. Section 2 introduces dephasing effects in 2D TIs. The works fall under two categories: phenomenological investigation of dephasing effects on transport properties and latest development of mircosopic mechanisms of spin dephasing. In Section 3, we present how the dephasing process affects the transport properties in 3D TIs. Finally, a brief conclusion and an outlook for future dephasing research are given in Section 4.

2 Dephasing effects in 2D topological insulators

In this section, we focus on the dephasing effects in 2D TIs. First, we introduce dephasing effects on transport properties by phenomenological analysis. Jiang *et al.* showed that spin dephasing is the dominant edge scattering process in QSHE [63]. Next, we present the latest development of microscopic spin dephasing caused by the joint effects of puddles and normal dephasing mainly based on Refs. [67, 69].

2.1 Phenomenological investigation of dephasing effects on transport properties

A QSH state is featured by helical edge states. Previous theories predicted the quantized longitudinal resistance plateaus [16]. However, the milestone QSHE experiment shows that the quantized longitudinal resistance plateaus can be only observed for short samples with a size of about 1 μm [17], which gives close to the value $h/(2e^2)$. When the sample size reaches about 20 μm, the longitudinal resistance deviates from the value $h/(2e^2)$ and increases strongly. Afterwards, these phenomena are confirmed by two independent groups in InAs/GaSb QWs [38] and WTe_2 [39]. Furthermore, the latter also manifested that the longitudinal resistance increases linearly with the sample length regardless of the sample width. Previous theoretical studies are short of understanding of dephasing effects in QSHE. In the following, we describe that how the dephasing effects influence on the transport properties of a QSH state.

2.1.1 Longitudinal resistance behaviours

First, we review the dephasing effects on the longitudinal resistance in the helical edge states. The work starts from considering a six-terminal device as shown in Fig. 1(a). For simplicity, QSHE is regarded as two copies of QHE with opposite Chern numbers. The Hamiltonian of such a QSHE device in the tight binding model can be described as [72]

$$H = -\Big[\sum_{\langle \boldsymbol{ij}\rangle\sigma} t\mathrm{e}^{\mathrm{i}\eta(\sigma)\phi_{\boldsymbol{ij}}} c^{\dagger}_{\boldsymbol{i}\sigma} c_{\boldsymbol{j}\sigma} + H.c.\Big] + \Big[\sum_{\boldsymbol{ik}\sigma} \epsilon_{k\sigma} a^{\dagger}_{\boldsymbol{ik}\sigma} a_{\boldsymbol{ik}\sigma} + (t_{k\sigma} a^{\dagger}_{\boldsymbol{ik}\sigma} c_{\boldsymbol{i}\sigma} + H.c.)\Big], \quad (1)$$

where the first term describes the central region and six terminals. $c^{\dagger}_{\boldsymbol{i}\sigma}$ ($c_{\boldsymbol{i}\sigma}$) is the creation (annihilation) operator of an electron on the lattice site $\boldsymbol{i}$ in the central region, $t = \hbar^2/(2m^*a^2)$ is the nearest hopping matrix element with the lattice constant a, $\eta(\sigma)\phi_{\boldsymbol{ij}}$ is the spin-dependent phase with $\eta(\sigma) = \pm 1$ for the real spin up ($\sigma =\uparrow$) and down ($\sigma =\downarrow$) due to SOC [73]. The summation of four $\phi_{\boldsymbol{ij}}$ along each unit satisfies $\sum \phi_{\boldsymbol{ij}} = eB_{eff}a^2/\hbar$, here B_{eff} is an effective magnetic field caused by SOC. The second term represents the Hamiltonian of the ideal virtual leads and the coupling with central regions. $a^{\dagger}_{\boldsymbol{ik}\sigma}$ ($a_{\boldsymbol{ik}\sigma}$) is the creation (annihilation) operator of an electron in the ideal virtual leads connected with site $\boldsymbol{i}$. The size of the central region is $(L + 2M) \times W$ as shown in Fig. 1(a). The longitudinal resistance is computed by applying the Landauer–Büttiker formalism combined with the non-equilibrium Green function method [74–76]. Dephasing effects only take place in the central region. In the numerical study, the dephasing effect is introduced by Büttiker's virtual probes [76, 77] with the dephasing strength Γ, which is directly related to the phase coherence length L_ϕ [78]. The total current under dephasing effects contains the contributions of phase-coherent part and phase-incoherent part. The ratio of the phase-incoherent part increases along with the increase in dephasing strength Γ. At a certain value Γ, both parts could have equal percentage, and the system size L is recognized to be equal to the phase coherent length L_ϕ. A small bias V_{14} between lead 1 and lead 4 is added to drive a current I_{14} flowing along the longitudinal direction.

The longitudinal resistance $R_{14,23} \equiv V_{23}/I_{14}$ versus B_{eff} for the normal and spin dephasing with several isolated dephasing strength Γ is shown in Figs. 1(b, c). The solid lines in both figures represent the perfect quantized plateaus of a QSH state at $h/(2\nu e^2)$ when $\Gamma = 0$. Here, the index ν ($\nu = 1, 2, 3, \ldots$) is responsible for multi-channels. When increasing the dephasing strength Γ, the normal dephasing has a slight impact on the longitudinal resistance $R_{14,23}$. The quantized plateaus is almost preserved in Fig. 1(b). That's a big contrast when introducing the spin dephasing in the central region. The longitudinal resistance $R_{14,23}$ in Fig. 1(c) deviates from the quantized plateaus seriously even with small Γ. In conclusion, the quantized plateaus in QSHE is robust against the normal dehasing but fragile with the spin dephasing. The two distinct behaviours of $R_{14,23}$ can be related to the concept of

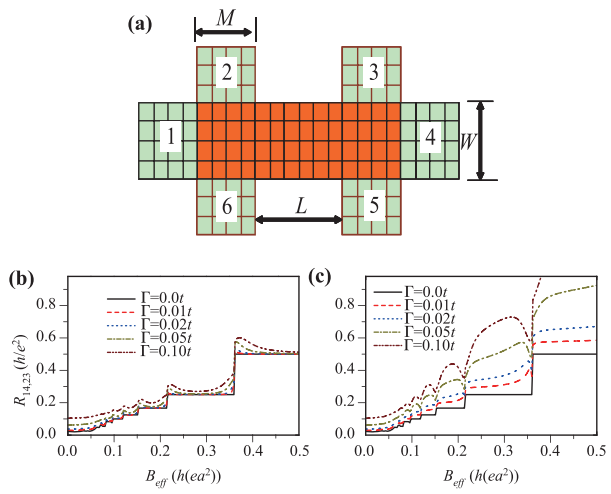

Fig. 1 **(a)** Schematic diagram for a six-terminal Hall bar sample, the gray (or red) area is the central region containing dephasing. **(b)** and **(c)** illustrate the longitudinal resistance $R_{14,23}$ vs B_{eff} in the presence of normal and spin dephasings, respectively. The parameters are $M = 24a$, $L = 32a$ and $W = 32a$. In all cases, the hopping matrix element is $t = 1$ and Fermi energy is $E_F = -3t$. Reproduced from Ref. [63].

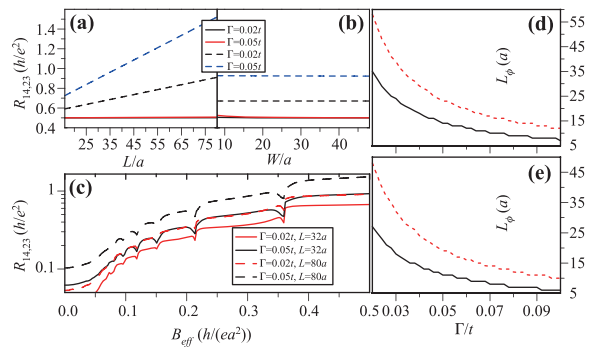

Fig. 2 **(a)** and **(b)** show $R_{14,23}$ vs. the sample length L with $W = 32a$ (a) and the width W (b) with $L = 32a$ (b), $M = 24a$, and $B_{eff} = 0.5$. The solid and dash lines are for the normal and spin dephasings, respectively. **(c)** $R_{14,23}$ vs. B_{eff} for different sample lengths L and spin-dephasing strengths Γ with $W = 32a$ and $M = 24a$. **(d)** and **(e)** show L_ϕ vs. Γ at $B_{eff} = 0.5$ (d) and 0.3 (e) with $W = 32a$. The solid and dotted curves in (d) and (e) are for the normal and spin dephasings. Reproduced from Ref. [63].

backscattering. Since normal dephasing doesn't flip spin, the carriers only lose phase memories. The backscattering is only allowed between two different edges of the sample. Thus, the backscattering is very weak except when the Fermi energy is near a Landau level center, and the quantized plateaus still sustains even with very large Γ. However, spin dephasing can flip a carrier's spin. A carrier can be scattered in one single edge. The backscattering is much stronger and the longitudinal resistance $R_{14,23}$ is much larger. In that case, the quantized plateaus is broken due to strong backscattering.

In addition, the phase coherence length L_ϕ is calculated to visualize the destruction of phase relevant to the dephasing strength Γ shown in Figs. 2(d) and (e). Specifically, spin dephasing is common due to magnetic impurities and nuclear spin fluctuations in a realistic system [64, 65], etc., and hence, the quantized plateaus of longitudinal resistance of QSHE only exists in systems with sample size smaller than spin dephasing length L_ϕ. This is the reason why the quantized plateau cannot be observed in samples with large lengths [17, 38, 39]. The plateau of $R_{14,23}$ is preserved under normal dephasing effects regardless of the sample length L or the width W [see Fig. 2(b)]. However, for spin dephasing, $R_{14,23}$ is linearly increasing with the sample size L and almost keeps stable with the disorder W [see Fig. 2(a)]. It turns out the quantized plateaus cannot sustain for large samples. $R_{14,23}$ approaches the plateau characteristics with the dephasing strength Γ altered, although the plateau may deviate from the idealized quantized one of $h/(2\nu e^2)$ without spin dephasing [see Fig. 2(c)]. The feature is consistent with the experimental results. To sum up, the experimental findings from the perspective of the behavior of $R_{14,23}$ and its dependence on temperature and sample size can be explained by spin dephasing effects [17].

2.1.2 Quantized spin Hall resistance

Since the quantized plateaus of longitudinal resistance $R_{14,23}$ cannot be observed for macroscopic samples due to spin dephasing, it is required to find an observable quantized quantity to reflect the topological nature of the QSHE. Here, spin Hall resistance $R_s = (V_{i\uparrow} - V_{i\downarrow})/I_{14}$ is defined as a new quantized quantity and shown in Figs. 3(c) and (d). Notice though, that the quantized plateaus of R_s is preserved regardless of strong normal or spin dephasing. Specifically, the sample length at $\Gamma = 0.1t$ exceeds L_ϕ by one order of magnitude, R_s is well quantized. Thus, the plateaus of spin Hall resistance is visible in macroscopic QSHE systems. The robustness of R_s against both dephasing mechanisms traces an analogy with the Hall resistance plateaus in QHE. The origin is explained below. In Figs. 3(a) and (b), the chemical potential along the boundary is present. The chemical potentials are always spin-independent with $V_{1\sigma} = -V_{4\sigma} = V$ in the left(right) leads. However, the chemical potential $V_{c\sigma}$ is spin-dependent in the central region. The left leads inject both spin-up and spin-down electrons. Since normal dephasing doesn't flip spin, the spin-up electron flows into the right lead and the spin-down one goes back to the left lead [see Fig. 3(a)]. When the spin dephasing is introduced, the flow directions of electrons are random due to spin flip. The chemical potential $V_{c\sigma}$ descends along the longitudinal direction as shown in Fig. 3(b). Nevertheless, the current I_{14} necessitates a constant, and hence stable $V_{c\uparrow} - V_{c\downarrow}$ at any position along the sample and the spin dephasing strength Γ, since the current I_{14} is carried

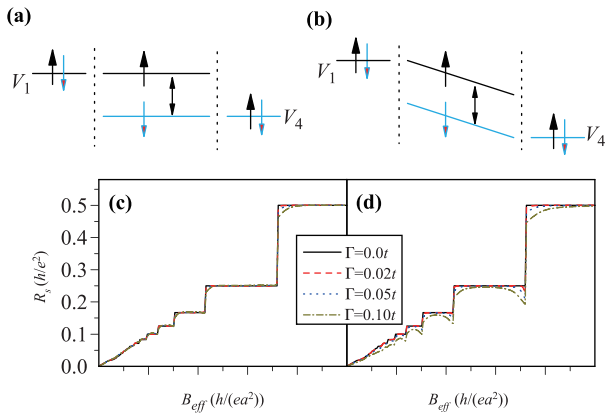

Fig. 3 **(a)** and **(b)** are the schematic diagrams for the chemical potential along a given boundary with (a) and without (b) spin dephasing. **(c)** and **(d)** plot the spin Hall resistance R_s vs. B_{eff} for the normal dephasing and the spin dephase case, respectively. The parameters are $M = 24a, L = 32a$ and $W = 32a$. Reproduced from Ref. [63].

by the edge states between $V_{c\uparrow}$ and $V_{c\downarrow}$. Therefore, the spin Hall resistance $R_s = (V_{2\uparrow} - V_{2\downarrow})/I_{14}$ is quantized in macroscopic samples. The voltage difference of $V_{2\uparrow} - V_{2\downarrow}$ is observable experimentally [79–84].

2.2 Latest development of microscopic mechanisms of spin dephasing

In above subsection, we have introduced the significant influences on transport properties in QSHE caused by spin dephasing effects. Here, we describe several joint effects resulting in spin dephasing mechanisms. In the past, it is known that spin dephasing can come from a single mechanism, e.g. magnetic impurities or spin fluctuation [64, 65]. Apart from the single mechanism, several joint effects which lead to spin dephasing mechanisms in the extended edge states in QSHE generate much interest recently: (1) electron–electron interaction and the momentum linear k-order Rashba SOC for a extended QSH state [66, 67]; (2) the k^3-order Rashba SOC term and electron–phonon interaction for a extended QSH state [68]. Nevertheless, latest experiments study QSHE on a local scale, since puddles widely exist in doped semiconductor hetero-structures due to the constraints of inhomogeneity of donors and acceptors inevitably introduced by sample growth [17, 43, 85]. These researches identify the enhancement of spin dephasing in the helical edge states by puddles. Thus, we turn to discuss the latest developments of puddles enhanced microscopic mechanisms of spin dephasing which rely on the joint effects.

2.2.1 Puddles combined with electron–phonon interaction enhanced spin dephasing mechanism

In confined QSH QDs, the combination of k-order Rashba SOC and electron–phonon interaction provides an effective spin dephasing mechanism. Hereinafter, Rashba SOC term is treated as perturbation. The whole Hamiltonian of our model, a 4×4 matrix, is written as

$$H = \begin{pmatrix} h(k) & h_R \\ h_R^\dagger & h^*(-k) \end{pmatrix}. \tag{2}$$

A metallic puddle is simulated in QSHE as a QSH QD, described by the massive Dirac Hamiltonian as shown in Fig. 4(a). The above matrix element $h(k)$ denote the Hamiltonian for the spin-up part, here $h^*(-k)$ is the time-reversal counterpart. The Hamiltonian $h(k)$ can be represented in the cylindrical coordinates as follows:

$$h(k) = \begin{pmatrix} M(\boldsymbol{r})v^2 & -\mathrm{i}\hbar v \mathrm{e}^{-\mathrm{i}\theta}\left(\frac{\partial}{\partial r} - \mathrm{i}\frac{1}{r}\frac{\partial}{\partial \theta}\right) \\ -\mathrm{i}\hbar v \mathrm{e}^{\mathrm{i}\theta}\left(\frac{\partial}{\partial r} + \mathrm{i}\frac{1}{r}\frac{\partial}{\partial \theta}\right) & -M(\boldsymbol{r})v^2 \end{pmatrix} \tag{3}$$

with the mass term

$$M(\boldsymbol{r}) = \begin{cases} m_1, & r > R_0, \\ -m_2, & r < R_0, \end{cases} \tag{4}$$

where m_1 and m_2 has positive values and v is the Fermi velocity. When the sign of the mass $m(\boldsymbol{r})$ is different inside

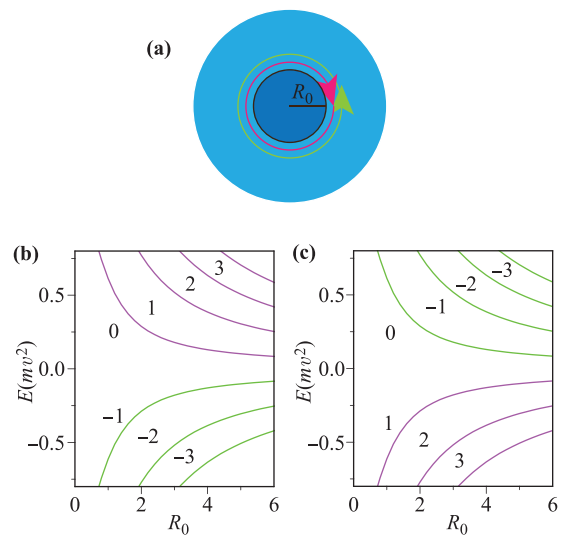

Fig. 4 **(a)** Schematic plot of a two-dimension QSH QD. Electrons with different spin directions have opposite angular momenta and run oppositely along the edge. The disk represents a QSH QD which is described by the two-dimensional massive Dirac Hamiltonian. The sign of mass term in Dirac Hamiltonian differs around the radial boundary R_0 in the QSH QD. And there exists a pair of helical states circulating along the boundary. **(b)** Energy levels of spin-up part of topological boundary of a QD versus radius R_0. Different curves represent different rotation directions. In (b) and (c), $m = v = \hbar = 1$; **(b)** and **(c)** are the energy levels of spin-up and spin-down parts, respectively. Reproduced from Ref. [69].

and outside the boundary $r = R_0$, there always exists a bound solution at $r = R_0$ [86, 87]. Thus, one call the mass sign change at $r = R_0$ a topological boundary. The bound solution is a pair of helical states circulating around the disk due to the TRS, as shown in Fig. 4(a). Since the z-component of the total angular momentum $j_z = -\mathrm{i}\hbar\partial_\theta + (\hbar/2)\sigma_z$ can be a good quantum number [88], one would like to adopt $\psi_{n\sigma} = |n\sigma\rangle$ to label the helical state in the QSH QD. $n(n \in \{0, \pm1, \pm2, \ldots\})$ is the angular momentum in z direction.

A Rashba SOC term h_R may come from the axial symmetry breaking [89] and $h_R^\dagger$ is the time-reversal counterpart of h_R. Specifically, the electric potential at the boundary of puddles causes a perpendicular electric field affecting the Rashba SOC, which is present in the cylindrical coordinate with the strength α below:

$$h_R = \begin{pmatrix} \alpha \mathrm{e}^{-\mathrm{i}\theta}\left(\dfrac{\partial}{\partial r} - \mathrm{i}\dfrac{1}{r}\dfrac{\partial}{\partial\theta}\right) & 0 \\ 0 & 0 \end{pmatrix}. \tag{5}$$

The eigenvector of Eq. (2) is taken as $\Psi = (\psi_{n,\uparrow}, \psi_{n',\downarrow})^{\mathrm{T}}$. $\psi_{n,\uparrow}$ and $\psi_{n',\downarrow}$ are spinors associated with the spin-up and spin-down states, respectively. The bound solutions of $h(k)$ are solved when $r > R_0$ and $r < R_0$. By introducing the spherical spinor waves $\psi_{n\uparrow} = \left(\begin{smallmatrix} f_n(r)\mathrm{e}^{\mathrm{i}n\theta} \\ g_n(r)\mathrm{e}^{\mathrm{i}(n+1)\theta}\end{smallmatrix}\right)$ into the Hamiltonian $h(k)$ in Eq. (3), the Hamiltonian can be separated into two parts. The radial part of $h(k)$ becomes

$$h_r = \begin{pmatrix} m_1 v^2 & -\mathrm{i}\hbar v\left(\dfrac{\partial}{\partial r} + \dfrac{n+1}{r}\right) \\ -\mathrm{i}\hbar v\left(\dfrac{\partial}{\partial r} - \dfrac{n}{r}\right) & -m_1 v^2 \end{pmatrix}. \tag{6}$$

Only bound states near the junction are considered for $\psi_{|r=+\infty} = 0$ here. Assume a trial solution $\psi_{n,\uparrow} = (\psi_1, \psi_2)^{\mathrm{T}}\mathrm{e}^{-\lambda_1 r}$. λ_1 should be positive and real to meet the conditions of $r = +\infty$. The pure imaginary solutions, when $m_1 v^2 < E_{n\uparrow}$, indicate that the corresponding wave functions spread all over the space. By substituting $g_n = \frac{-\mathrm{i}\hbar v(\partial r - \frac{n}{r})}{m_1 v^2 + E_{n\uparrow}} f_n$ into the radial Hamiltonian h_r, they can obtain the modified Bessel equation of f_n and the corresponding spinor $\psi_{n\uparrow} = A\left(\begin{smallmatrix} \frac{\mathrm{i}\hbar v\lambda_1}{E_{n\uparrow} - m_1 v^2} K_n(\lambda_1 r)\mathrm{e}^{\mathrm{i}n\theta} \\ K_{n+1}(\lambda_1 r)\mathrm{e}^{\mathrm{i}(n+1)\theta}\end{smallmatrix}\right)$, which requires $\lambda_1 = \frac{\sqrt{m_1^2 v^4 - E_{n\uparrow}^2}}{\hbar v}$. $K_n(\lambda_1 r)$ is the modified Bessel function of second kind. Next, a similar procedure should be adopted in the region $r < R_0$. The solution is $\psi_{n\uparrow} = B\left(\begin{smallmatrix} \frac{-\mathrm{i}\hbar v\lambda_2}{m_2 v^2 + E_{n\uparrow}} I_n(\lambda_2 r)\mathrm{e}^{\mathrm{i}n\theta} \\ I_{n+1}(\lambda_2 r)\mathrm{e}^{\mathrm{i}(n+1)\theta}\end{smallmatrix}\right)$ and $\lambda_2 = \frac{\sqrt{m_2^2 v^4 - E_{n\uparrow}^2}}{\hbar v}$ with $m_2 v^2 > E_{n\uparrow}$ (A, B are the normalization factors). $I_n(\lambda_2 r)$ is the modified Bessel function of first kind. By requiring the continuity at $r = R_0$, the solution is a transcendental equation of $E_{n\uparrow}$ as (for simplicity, they take the mass $m_1 = m_2 = m$ and thus $\lambda_1 = \lambda_2 = \lambda$)

$$\frac{E_{n\uparrow}}{mv^2} = \frac{K_{n+1}(\lambda R_0)I_n(\lambda R_0) - K_n(\lambda R_0)I_{n+1}(\lambda R_0)}{K_{n+1}(\lambda R_0)I_n(\lambda R_0) + K_n(\lambda R_0)I_{n+1}(\lambda R_0)}. \tag{7}$$

The angular momentum is labeled as $n' \in \{0, \pm1, \pm2, \ldots\}$ in the spin-down case. For a system with TRS, the Kramers pair $\psi_{n\uparrow}$ and $\psi_{n'\downarrow}$ have the opposite angular momentum, i.e., $n' = -n$, so the transcendental equation for energies of $h^*(-k)$ is written as

$$\frac{E_{n'\downarrow}}{mv^2} = \frac{K_{n'-1}(\lambda R_0)I_{n'}(\lambda R_0) - K_{n'}(\lambda R_0)I_{n'-1}(\lambda R_0)}{K_{n'-1}(\lambda R_0)I_{n'}(\lambda R_0) + K_{n'}(\lambda R_0)I_{n'-1}(\lambda R_0)}. \tag{8}$$

The energy levels of topological boundary of a QSH QD verse radius R_0 are shown in Figs. 4(b, c) numerically. The smaller R_0 is, the more discrete the energy levels become. Specifically, they can deduce $E_{n\uparrow(\downarrow)} = \pm\frac{(n+\frac{1}{2})\hbar v}{R_0}$ when $R_0 \to \infty$. For an arbitrary angular momentum n, the two states have opposite velocities forming a pair of helical bound states (see Fig. 4). Furthermore, the energy spectrum has the Dirac-like form of $E_{n\uparrow(\downarrow)} = \pm\hbar v k$ by defining a new wavevector $k = \frac{(n+\frac{1}{2})}{R_0}$. Thus, the asymptotic solution can recall the extended helical edge states.

Here, we review how the Rashba SOC and electron–phonon interaction affect backscattering of bound helical edge states in a TI QD. In this model, Rashba SOC is treated as perturbation. Thus, the scattering matrix $h^R_{n\uparrow n'\downarrow} = \frac{\langle n\uparrow|h_R|n'\downarrow\rangle}{|E_{n\uparrow} - E_{n'\downarrow}|}$ can be calculated. The whole scattering matrix contains two parts: the inside region $r < R_0$ and the outside region $r > R_0$. To get the nonzero value, the angular part of the integration must meet $n' = n + 1$ and thus $E_{n+1\downarrow} = -E_{n\uparrow}$. In other words, the scattering only occurs between two states when their angular momentum differ by one. Though $h^R_{n\uparrow n+1\downarrow}$ is nonzero, backscattering is prohibited for a physical system due to the energy conservation when only Rashba SOC is considered. The energy difference of the initial and final states can be overcome by considering phonons. Thus, both the SOC and phonon-electron interaction are essential for inelastic backscattering in our model. The temperature-dependent spin dephasing rate can be used to describe the inelastic backscattering [90] which is written as $1/\tau_s = 8\pi T\int_0^\infty \mathrm{d}\omega\alpha_s^2 F(\omega)\frac{\partial p(\omega)}{\partial T}$. $\alpha_s^2 F(\omega) = \frac{1}{\Delta}|g_0|^2|h^R_{n\sigma n'\sigma'}|^2\delta(\Delta - \hbar\omega)\mathrm{e}^{-\frac{|\hbar\omega - \hbar\omega_0|^2}{2\xi^2}}$ is the spin-flip Eliashberg function [90, 91], here $\Delta = |E_{n\sigma} - E_{n'\sigma'}|$ denotes the energy difference, ξ is the width of optical phonon energy, $p(\omega) = [\exp(\hbar\omega/(k_B T)) - 1]^{-1}$ and $\hbar\omega$ represents the optical phonon energy. The local electron–phonon scattering matrix is taken as $g_0 = \sqrt{\frac{\hbar C_{op}^2/a^2}{2\rho_A V\omega}}$ with the optical deformation potential C_{op}, the atomic mass density ρ_A and the lattice constant a [92].

So far, the effective spin dephasing due to the joint effect of linear k-order Rashba SOC and the electron–phonon interaction in local helical edge states with TRS preserved has been demonstrated. Figure 5 shows the spin dephasing relaxation time $1/\tau_s$ verse the radius R_0 in two typical QWs: HgTe/CdTe QWs and InAs/GaSb QWs. The puddles in this model has the size of tens-of-nanometer.

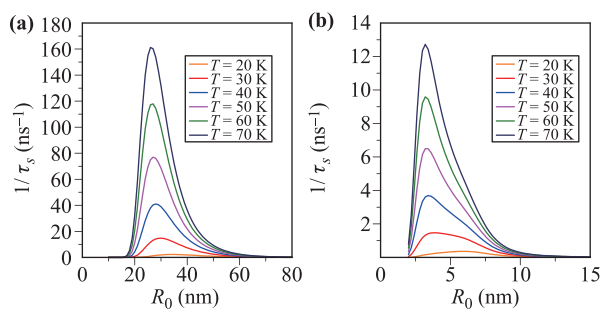

Fig. 5 Spin dephasing relaxation time versus puddle size R_0 of **(a)** HgTe/CdTe QWs and **(b)** InAs/GaSb QWs. In (a), $mv^2 = -24.8$ meV, $\hbar v = 333.6$ meV·nm, $\omega_0 = 17$ meV [93]; In (b), $mv^2 = -7.8$ meV, $\hbar v = 37$ meV·nm, $\omega_0 = 25$ meV [94]; and the Fermi energy $E_F = 0$, the optical deformation potential $C_{op} = 20$ eV, Rashba coupling constant $\alpha = 70$ meV·nm [95], phonon frequency width $\xi = 3.5$ meV in both cases. Reproduced from Ref. [69].

Notice that, for an arbitrary temperature T, $1/\tau_s$ varies with the puddle sizes and has a peak when the level spacing energy approaches the phonon frequency ω_0. The peak shows that the spin dephasing is much stronger and the spin dephasing time is much shorter. Pay attention to the non-monotonic behaviour of the dephasing rate in Fig. 5. The scattering is very weak at both ends of the curves, but has different origins at different end. First, the large energy spacing between neighboring local edge states is scarcely overcome by the optical phonon energy for small puddles. On the other hand, for puddles with large size, the edge states tend to be extended, and this is beyond the scope of our model. In such case, it has been proved that the combination of linear k-order Rashba SOC and normal dephasing cannot contribute to the spin dephasing in extended edge states [68]. In a realistic system, there always exist puddles due to inhomogeneity caused by long-range disorder or the external gate. The extended helical edge states at the boundary of sample can couple with the local helical edge states in the puddle several times. Thus, the electrons in extended helical edge states can also undergo the inelastic backscattering through the tunneling.

2.2.2 Puddles combined with electron–electron interaction enhanced spin dephasing mechanism

Except for the puddles combined with electron–phonon enhanced spin dephasing mechanism, the robustness of the quantized conductivity for free-electrons could be destroyed by electron–electron scattering concerning with the puddles as well [67]. The puddles are stimulated by the QDs (see Fig. 6). TRS guarantees the quantization of conductivity G_0 with value e^2/h each edge. Each edge has a pair of the right-moving (R) and left-moving (L) carrier. Whereas there is no backscattering in the extended edge states, electron–electron interactions in the QDs lead to inelastic backscattering. They consider the long-range

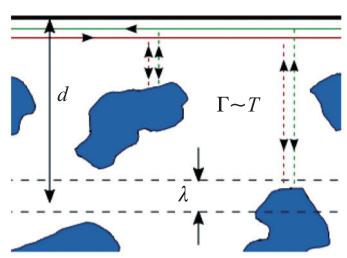

Fig. 6 Electrons moving along a helical edge tunnel in and out of puddles created by the inhomogeneous charge distribution in the heterostructure. In the puddles, electrons may undergo inelastic backscattering. Reproduced from Ref. [67].

Coulomb interaction only in QDs which they assume respects the TRS. The long-range Coulomb interaction may cause two backscattering processes: one is for one electron (RR-RL) and the other one is for two electrons (RR-LL), which gives the conductivity correction δG_1 and δG_2. Specifically, $\delta G_1 \propto T^4$ and $\delta G_2 \propto T^6$ in low temperature limit [67]. The helical edge states can go through the inelastic backscattering via the coupling with the QDs via a point contact.

3 Dephasing effects in 3D topological insulators

In this section, we discuss how the dephasing effects influence the transport properties in 3D TIs. One of the hallmark of 3D TIs is the particular chiral spin texture in the 2D surface. Thus, the microscopic mechanisms of spin dephasing in 3D TIs are quite different from the case in QSHE. Rashba SOC is not essential for spin flip due to the intrinsic spin texture [49, 58]. However, electrons in the helical edge states can only propagate forward and backward along the edge with spin perpendicular to the momenta in QSHE. In a realistic sample, impurities always exist to some degree. Scattering by impurities can change a carrier's momenta, hence its spin orientation due to spin-momentum locking mechanism. The joint effect of impurities and normal dephasing commonly exist in 3D TIs, and analogy to the 2D case, can cause spin dephasing. Such spin dephasing effects have been observed in recent experiments [96–99]. On the other hand, the variable-range-hopping (VRH) transport due to the wide existence of puddles results in a new spin dephasing mechanism. In the following, we introduce the recent developments of dephasing effects in 3D TIs mainly based on Refs. [70, 71].

3.1 Impurities induced dephasing effects on the helical surface states

3D TIs are characterized by the gapless surface states which are protected by the bulk gap. Recent researchers have focused on the experiments of the alloy $BiTl(S_{1-x}Se_x)_2$ [96–99]. A topological quantum phase

transition (QPT) would take place at $x_c \approx 0.5$ from a trivial state ($TlBiS_2$) to a topological state ($TlBiSe_2$) when increasing the S/Se ratio x. It is found that the surface states in $BiTl(S_{1-x}Se_x)_2$ acquires an unexpected mass for $0.6 < x < 0.9$ which is so-called anomalous Dirac gap at the Γ point. It is thought that a Dirac gap in helical surface states occurs when TRS is broken. However, zero z-spin component in $BiTl(S_{1-x}Se_x)_2$ by spin-resolved ARPES indicates that no magnetic order exists in the samples and thus TRS is preserved. The existing accounts fail to resolve the contradiction between the theory and experimental result. Besides, it reminds us the importance of the impurities in view of the fact that this gap grows when increasing the S concentration [97]. The anomalous "gap-like" feature arouses the investigation of the microscopic spin dephasing in the helical surface states of 3D TIs with TRS. Liu *et al.* found that the phenomenon can be explained by the spin dephasing effects in the helical surface states. Moreover, they intensively studied the spin dephasing effects on transport properties in 3D TIs.

3.1.1 Origin of the normal dephasing

An incident particle is reflected along a random path "1" ($\alpha \to 2 \to 1 \to \beta$). In the phase coherent regime, there is a time-reversed path "1R" ($\beta \to 1 \to 2 \to \alpha$). The schematic plot of the two paths is shown in Fig. 7. In a realistic system, an electron is scattered not only by the impurities but also by the phonons or other electrons which are two typical dephasing origins. Once the dephasing mechanism is considered, the quasiparticles which go through path "1" and time-reversed path "1R" gain a random phase difference $\delta\varphi$. Traditionally, the random phase uncertainty at the finite temperature satisfies $\langle\delta\varphi^2\rangle \propto T^\alpha$ for parabolic-like massive carriers, e.g., $\alpha = 1$ for electron–electron interaction [62, 100] and $\alpha = 2$ for electron–phonon interaction [61, 101]. However, the situation is very different in Dirac electron systems. They show the temperature dependence of $\delta\varphi$ for both dephasing mechanisms below.

Firstly, the electron–phonon interaction induced dephasing effects is considered. The random phase uncertainty $\delta\varphi$ is associated with the temperature-dependent dephasing rate τ_i^{e-ph} by relation $\langle\delta\varphi^2\rangle = \frac{\tau_0}{\tau_i^{e-ph}}$. τ_0 is the time between two adjacent scatters. The dephasing rate due to electron phonon coupling is determined by the Eliashberg function (introduced in Section 2.2.2) [101]:

$$\frac{1}{\tau_i^{e-ph}} = 2\pi \int \frac{\alpha^2 F(\omega)}{\sinh(\frac{\hbar\omega}{k_B T})} \mathrm{d}\omega, \tag{9}$$

where T is temperature. For simplicity, only non-Umklapp scattering process is included. The low temperature regime with $k_B T \ll \hbar v_L q_0$ and the high temperature regime with $\hbar v_L q_0 \ll k_B T < \hbar\theta_D$ are considered in view of high Debye frequency θ_D. Here, v_L denotes the longitudinal phonon velocity and q_0 represents the longitudinal phonon self-energy correction. In the low temperature regime, the dephasing rate τ_i^{e-ph} shows the T^3 dependence as $\frac{1}{\tau_i^{e-ph}} \propto \frac{(k_B T)^3}{\hbar\theta_D(\hbar v_L q_0)^2}$ [70]. Compared to this, the dephasing rate in the high temperature regime, displays the $T\ln(T)$ dependence as $\frac{1}{\tau_i^{e-ph}} \propto \frac{k_B T}{\hbar\theta_D}\log(\frac{k_B T}{\hbar v_L q_0})$ [70]. Thus, the random phase $\langle\delta\varphi^2\rangle$ shows the same temperature dependence with $\frac{1}{\tau_i^{e-ph}}$ due to Eq. (9).

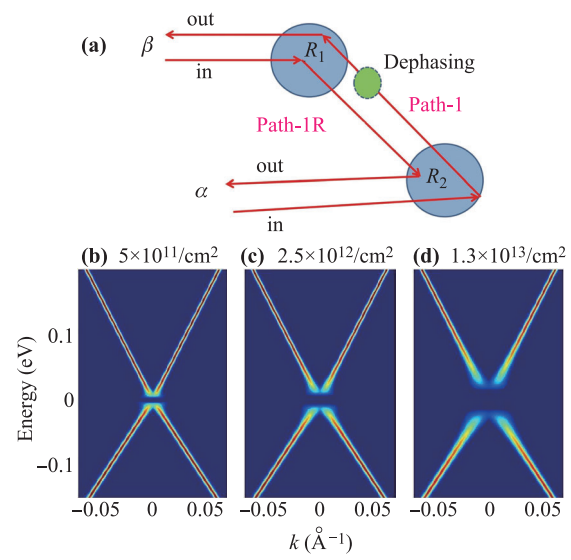

Fig. 7 **(a)** Dephasing effect on the time reversal counterpart paths, shown as Boltzmannian trajectories. **(b–d)** The quasiparticle dispersion of TI surface states under different charge impurity concentration. The bandwidth broadening effect, due to charge impurity scattering, lead to dramatic band distortion around the Dirac point. From (b) to (d), the charge impurity concentration gradually increase from $n_i = 5 \times 10^{11}/\mathrm{cm}^2$ (b) to $n_i = 1.3 \times 10^{13}/\mathrm{cm}^2$ (d), the dispersion around Dirac point become increasing blurred. Reproduced from Ref. [70].

Next, the electron–electron interaction induced dephasing mechanism is introduced. In particular, the random phase uncertainty $\delta\varphi$ between two counterpart paths is shown in Fig. 7(a). Assume the electrons travel in the environment with a time-dependent electric potential $V_I(x(t))$, so the phase uncertainty can be expressed as $\langle\delta\varphi^2\rangle = \iint \frac{\mathrm{d}t\,\mathrm{d}t'}{\hbar^2}[\langle V_I(x_1(t))V_I(x_2(t'))\rangle - \langle V_I(x_1(t))\rangle\langle V_I(x_2(t'))\rangle]$. Electron-electron induced potential has the form $V_I(x(t)) = \int \frac{e\hat{\rho}(\boldsymbol{r},t)}{|\boldsymbol{x}(t)-\boldsymbol{r}|}\mathrm{d}^2\boldsymbol{r} = \int \frac{e\hat{\rho}(\boldsymbol{q},t)}{2\pi q}\mathrm{e}^{-\mathrm{i}\boldsymbol{q}\boldsymbol{x}(t)}\mathrm{d}^2\boldsymbol{q}$. By applying the RPA approximation [100], the random phase has the form $\langle\delta\varphi^2\rangle \approx \frac{e^2 k_B T d_0}{(2\pi)^4 v_f \sigma\hbar^2}$ [70]. Here, σ denotes the conductivity, v_f is the Fermi velocity and d_0 is the skin depth of helical surface states. It is found that the random phase still linearly depends on temperature.

3.1.2 Backscattering cross section

In this section, we discuss the dephasing effects in 3D TIs. The main focus is the metallic surface states which are

the hallmark of the 3D TIs here. The helical surface states of the 3D TIs are described by the two-component Dirac Hamiltonian as [70]

$$H(\boldsymbol{k}) = s\hbar v_f(\hat{\boldsymbol{z}} \times \boldsymbol{k}) \cdot \sigma, \tag{10}$$

where v_f is the Fermi velocity, $\sigma = (\sigma_x, \sigma_y)$ are Pauli matrix for real spin, and $s = \pm 1$ represents the up and bottom surface, respectively. By defining a new wavevector $\tilde{\boldsymbol{k}} = \hat{\boldsymbol{z}} \times \boldsymbol{k}$, the Hamiltonian is rewritten as $H(\boldsymbol{k}) = \hbar v_f \tilde{\boldsymbol{k}} \cdot \sigma$ to keep it compact and replace $\tilde{\boldsymbol{k}}$ as $\boldsymbol{k}$ for generality. In the following part, only the up surface states with $s = 1$ is considered. The eigenstates of the top surface can be expressed in the plane wave basis as $\varphi_{\pm,\boldsymbol{k}}(\boldsymbol{r}) = \frac{1}{\sqrt{2}}(1, \pm e^{i\theta_{\boldsymbol{k}}})^{\mathrm{T}} e^{i\boldsymbol{kr}}$, here $\pm$ denotes the particle and hole carrier respectively and $\theta_{\boldsymbol{k}} = \arctan \frac{k_y}{k_x}$ represents the direction angle. The dephasing effects in 3D TIs by scattering theory are explained below.

Considering the ultrarelativistic Dirac case, the asymptotic scattering spinon wave function is $\psi_{out}(\boldsymbol{r}) = \varphi_{\boldsymbol{k_{in}}}(\boldsymbol{r}) + e^{ikr} \frac{f(\theta_{out}, \theta_{in})}{\sqrt{r}} \binom{1}{e^{i\theta_{out}}}$, where $r = |\boldsymbol{r}|$, $k = |\boldsymbol{k_{in}}|$, $\boldsymbol{k_{in}}$ denotes the incident wave vector, the $f(\theta_{out}, \theta_{in})$ is the scattering amplitude, and the cross section $\sigma(\theta_{out}, \theta_{in}) = |f(\theta_{out}, \theta_{in})|^2$ [102]. Since θ_{out} differs θ_{in} by a π phase due to the perfect coherence, there is no backscattering theoretically (see detailed derivation below). The quasiparticles which go through path "1" and time-reversed path "1R" gain a random phase difference $\delta\varphi$ concerning with the dephasing effets. By analogy to the case in QSHE, the existence of the random phase uncertainty $\delta\varphi$ cannot give rise to the backscattering individually. In fact, only the combination of impurities and normal dephasing effects contributes to backscattering. In the following part, the above conclusion by calculating the scattering amplitude and backscattering cross-section are confirmed.

The dilute impurities with the potential $V(\boldsymbol{r} - \boldsymbol{R_i})$ is considered, here $\boldsymbol{R_i}$ denotes the i-th impurity location. If the effect of the scatter is not very strong, Born approximation can be used to compute the the scattering amplitude and backscattering cross-section below. The first-order scattering wave function [70] can be deduced far away from the finite potential range,

$$\psi_1 = \frac{2k e^{ikr} \Gamma(\boldsymbol{k_{out}}, \boldsymbol{k_{in}}, \boldsymbol{R}_i)(1 + e^{-i(\theta_{out} - \theta_{in})})}{v_f \sqrt{-i2\pi kr}} \begin{pmatrix} 1 \\ e^{i\theta_{out}} \end{pmatrix},$$

where $\Gamma(\boldsymbol{k_{out}}, \boldsymbol{k_{in}}, \boldsymbol{R_i}) = \int d\boldsymbol{r} e^{-i(\boldsymbol{k_{out}} - \boldsymbol{k_{in}}) \cdot \boldsymbol{r}} V(\boldsymbol{r} - \boldsymbol{R_i})$. The factor $(1 + e^{-i(\theta_{out} - \theta_{in})})$ in the first-order Born amplitude is zero due to the π phase. Even if a random phase $\delta\varphi$ is added to the wave function ψ_1, the first-order backscattering is still zero. Therein, no backscattering process takes place in the first-order Born approximation. Next, take the higher-order Born approximation into account. The second-order scattering process is related to the Boltzmannian trajectories in Fig. 7(a). Assume that the average distance l between two scatters $\boldsymbol{R_1}$ and $\boldsymbol{R_2}$ are much larger than the finite potential range, and set the orientation angle of $\boldsymbol{R_2} - \boldsymbol{R}_1$ as ϕ. The second-order scattering wavefunction contains contributions from two inteference paths [70]:

$$\psi_2 = \frac{2k e^{ikr} \Gamma^2(k, \boldsymbol{R}_1, \boldsymbol{R}_2)}{-i\pi v_f^2 \sqrt{r|\boldsymbol{R}_2 - \boldsymbol{R}_1|}} F(\theta_{out}, \phi, \theta_{in}) + T.R., \tag{11}$$

where the phase factor between two paths is $F(\theta_{out}, \phi, \theta_{in}) = \begin{pmatrix} 1 & e^{-i\theta_{out}} \\ e^{i\theta_{out}} & 1 \end{pmatrix} \begin{pmatrix} 1 & e^{-i\phi} \\ e^{i\phi} & 1 \end{pmatrix} \begin{pmatrix} 1 \\ e^{i\theta_{in}} \end{pmatrix}$, and the scattering strength is written as $\Gamma^2(k, \boldsymbol{R}_1, \boldsymbol{R}_2) = \int\int d\boldsymbol{r_1} d\boldsymbol{r_2} e^{i(\boldsymbol{k_{in}} \cdot \boldsymbol{r_1} - \boldsymbol{k_{out}} \cdot \boldsymbol{r_2} + k|\boldsymbol{r_2} - \boldsymbol{r_1}|)} V(\boldsymbol{r_1} - \boldsymbol{R_1}) V(\boldsymbol{r_2} - \boldsymbol{R_2})$. The first part in Eq. (11) represents the contributions of path "1" and the $T.R.$ part is related with path "1R" which is associated with the first part by replacing ϕ with $\pi + \phi$ and changes $\boldsymbol{R_1}$ for $\boldsymbol{R_2}$. The second-order Born amplitude is deduced as [70]

$$f_2(\theta_{out}, \theta_{in}) = \frac{4k(1 + e^{-i(\theta_{out} - \theta_{in})}) \Gamma^2(k, \boldsymbol{R}_1, \boldsymbol{R}_2)}{-i\pi v_f^2 \sqrt{|\boldsymbol{R}_2 - \boldsymbol{R}_1|}}. \tag{12}$$

The phase factor $[1 + e^{-i(\theta_{out} - \theta_{in})}]$ indicates that the backscattering is also eliminated in second-order Born approximation. To simulate the realistic environment, the dephasing mechanism is introduced with a random phase difference $\delta\varphi$ by phenomenological analysis. The second-order scattering cross-section after the angle average of ϕ is

$$\sigma(\pi + \theta_{in}, \theta_{in}) = \frac{8k^2 \Gamma^4 \langle \delta\varphi^2 \rangle}{\pi^2 v_f^4 |\boldsymbol{R_2} - \boldsymbol{R_1}|}. \tag{13}$$

In conclusion, two complementary roles are essential in the backscattering process of the helical surface states: impurities and normal dephasing process. The backscattering process cannot take place with either impurities or dephasing process alone. Notice though, that backscattering only exists in high-order Born approximation.

3.1.3 Anomalous "gap-like" feature

The anomalous gap in the helical surface states is manifested by the co-existence of impurities and normal dephasing process [70]. In order to understand the experimental results deeply, the effects of the impurities should be investigated in more details. The long-range Coulomb potential $V_L(\boldsymbol{r} - R_i) = \frac{\hbar v_f \Delta}{|\boldsymbol{r} - R_i|}$ is taken into account, here Δ represents the dimensionless potential intensity. The backscattering cross-section for long-range potential $\sigma_L(\pi + \theta_{in}, \theta_{in}) = \frac{8\Delta^4 \langle \delta\varphi^2 \rangle}{\pi^2 k^2 |\boldsymbol{R_2} - \boldsymbol{R_1}|}$ is inversely proportional to k^2, which indicates that the long-range Coulomb potential scattering occurs around the Dirac point. On the basis of Coulomb scattering, The quasiparticle lifetime is obtained from the transport cross section: $\frac{1}{\tau} = v_f n_i \sigma_T$, here n_i is the impurity concentration and $\sigma_T = \oint \sigma(\theta)(1 - \cos\theta) d\theta$ is the total cross section [70]. Furthermore, the quasiparticle lifetime τ is included in the imaginary part of self energy,

which is related to the Coulomb scattering and dephasing effect by [70]

$$-\mathrm{Im}\Sigma^R(k) = \frac{2n_i\xi^2}{\epsilon_k} + \frac{4n_i\xi^4}{\hbar\pi v_f^2\tau_\varphi\epsilon_k^2}, \tag{14}$$

where $\epsilon_k = \hbar v_f k$, the Fermi velocity $v_f = 4\times10^5$ m·s^{-1}, the coupling constant $\xi = \frac{e^2}{4\pi\varepsilon_0} \approx 10^{-9}$ eV·m, and a moderate dephasing strength with $\tau_\varphi \simeq 10^{-10}$ s is considered [103]. In Eq. (14), the first part is the scattering lifetime without dephasing, and the dephasing effect is present in the second part. The spectrum function is calculated as $A(k,w) = -2\mathrm{Im}G^R(k,\omega)$ with $G^R(k,\omega) = 1/[\omega - \epsilon_k - \Sigma^R(k)]$. The quasi-particle dispersion of TI surface states by altering the impurity density n_i, is shown in Fig. 7. The quasiparticle dispersion behaves in a linear fashion except the adjacent Dirac point. When the impurity density n_i increases, it seem to form a gap near Dirac point [especially in the Fig. 7(c)]. The band broadening effect is caused by the strong backscattering due to the combination of the normal dephasing and the long-range Coulomb potential. Thus, the anomalous Dirac gap in $BiTl(S_{1-x}Se_x)_2$ can be clearly explained. Due to the enhanced backscattering around the Dirac point, weak (anti-) localization in such systems can be largely affected.

3.2 Puddles induced dephasing effects on the helical surface states

The dominant source of phase relaxation is usually electron–electron interactions at low temperatures. However, the situation may be more complicated in 3D TIs. Liao *et al.* have reported a new dephasing mechanism in highly tunable $(Bi,Sb)_2Te_3$ thin films [71]. The phase coherent transport in such a 3D TI thin films can be tuned continuously from the bulk-conducting regime to the decoupled surface-transport regime. In the bulk-conducting regime, both the bulk and surface states are conducting well. As opposed to this case, the latter refers to the insulating bulk states and decoupled metallic surface states. In the bulk-conducting regime, experimental results have consistently shown the electron–electron induced dephasing rate $\tau_\phi^{-1} \propto T$. This is so-called Nyquist dephasing mechanism [104], showing a T-linear dependence (we also introduced it in Section 3.1.1). Whereas in the decoupled surface-transport regime, the measured dephasing rate has a sublinear power-law temperature dependence ($\tau_\phi^{-1} \propto T^{0.55}$), deviating seriously from the electron–electron scattering (see Fig. 8). The enhancement of dephasing effects at low temperatures are attributed to the joint effect of the helical surface states and localized charge puddles in the 3D bulk states. Mott's theory of VRH transport can be used to explain the abnormal behavior of dephasing rate [105], in which electrons hop between localized states at different locations by thermal activations. VRH transport is a phonon-mediated hopping process, and hence affects the dephasing rate which is present as $\tau_\phi^{-1} \propto T^p$ with $p = 2/(d+1)$. Thus, $p = 2/3$ and $p = 1/2$ stand for the VRH transport in 2D and 3D electron systems [71]. Therefore, given the hybrid of 2D surface states and 3D bulk puddles in 3D TI thin films, the theoretical value is consistent with the experimental result in view of dephasing rate.

4 Conclusions and outlook

Thus far, we have provided a brief summary of the latest developments of dephasing effects in 2D and 3D TIs based on reviewing our own dephasing studies and other related investigations. In 2D TIs, the quantized longitudinal resistance is seriously damaged by spin dephasing. Thus, the quantized longitudinal resistance plateaus can only be observed in a sample smaller than spin dephasing length. In particular, the mechanism of spin dephasing in

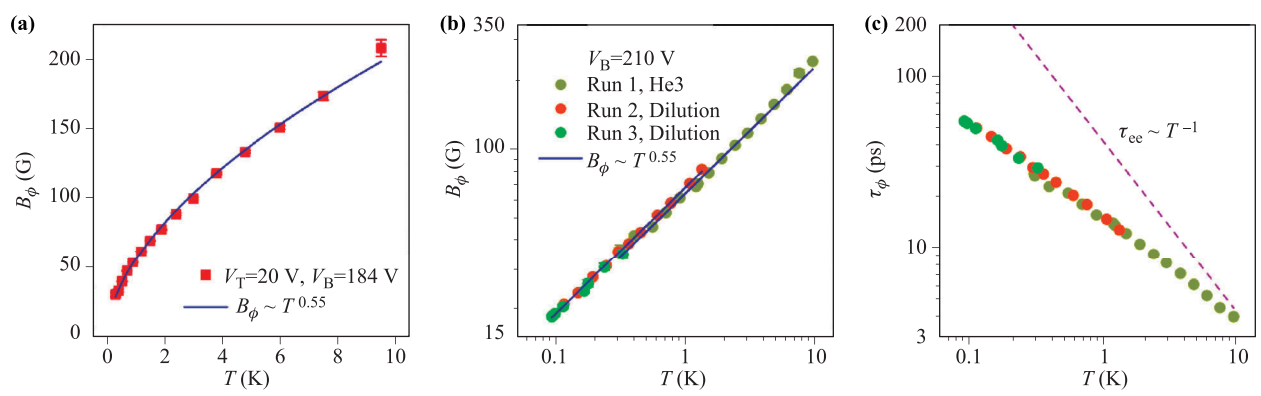

Fig. 8 Enhanced electron dephasing in the decoupled surface-transport regime. **(a)** Temperature dependence of dephasing field B_ϕ for a dual-gating case with $\alpha \approx 1$. The data can be well fitted to $B_\phi \propto T^p$ with $p = 0.55$. **(b)** Temperature-dependences of B_ϕ and the corresponding power-law fits for three cool-downs with single-gating. The extracted exponent p is same as the dual-gating case. **(c)** Dephasing time τ_ϕ of the bottom surface states as a function of temperature. The dashed line shows the estimated dephasing times due to the Nyquist electron–electron interactions. Reproduced from Ref. [71].

QSHE can originate from the joint effect of puddles and normal dephasing. In 3D TIs, it is meaningless to distinguish normal dephasing and spin dephasing due to the helical spin texture in the 2D surfaces, since any scattering process that changes the momentum can also change the spin direction. Thus, for 2D surface states in 3D TIs, the normal dephasing and spin dephasding are of the same origin. And backscattering takes place within TRS when considering the joint effect of impurities and normal dephasing. In spite of lots of significant progresses, there is abundant room for further studies in dephasing effects in TIs and other topological systems. We discuss the opportunities for dephasing studies in the future before the end of the review.

One of the remarkable theme is the intersect of topological phases and non-Hermitian systems which are open and out of equilibrium. A number of researchers make efforts to seek out topological non-Hermitian phases [106–114]. In particular, the system which go through dephasing process is indeed a non-Hermitian one. When applying spin dephasing into the 2D TIs, the quantized longitudinal resistance plateaus would be damaged. Instead, the spin Hall resistance is found to be a macroscopic observable quantity, which enlightens us on the finding of observable quantities in topological non-Hermitian phases.

On the other hand, searching for a more robust QSH state attracts much attention. Recently, Wang's group realized a "QSH-like" state by a bilayer of QAH insulators with opposite Chern numbers and the insulating layer sanwiched [115]. The two QAH insulators are applied by different coercive fields, hence have opposite magnetization. As a result, the two edge states counter-propagate with each other harboring opposite spin directions, which are very similar to the helical edge states in QSHE. More intriguingly, the quantized longitudinal resistance plateaus survives over macroscopic length scale even in strong disordered environment due to the spatial separation of two chiral edge states. Besides, it is convenient to tune the potentials of the top and bottom layers, respectively. Therefore, it enables the direct measurements of spin Hall resistance. Furthermore, the systems experience normal dephasing process when a lead is coupled with the single-layer QAH. Since the carrier propagates only in the single QAH layer, it will not change its chirality. The situation is such different when the lead is coupled with the whole sample. In this case, the chiral carriers enter into the lead, randomly lose their spin memories and turn into the opposite QAH layer, which suffers from the spin dephasing process. In other words, voltages can easily tune the types of dephasing effects in such a "QSH-like" state, which makes it a good platform for dephasing effect investigations.

Moreover, metal-insulator transition (MIT) is one of the most classical and important questions in physics. It is known that disorder can lead to the MIT [116]. When dephasing is applied in such systems, the universal class of phase transitions can be changed [117]. Questions have been raised about the dephasing effects on the MIT in topological materials [118–122]. In recent years, there has been an increasing interest in other topological materials, such as topological crystalline insulators [123], Weyl semimetals (WSMs) [124], and higher-order topological insulators (HOTIs) [125], etc. The dephasing effects on their transport properties, e.g., magnetoresistance, await a similar degree of development.

Acknowledgements We are grateful to Y. Q. Li, Q. F. Sun and S. G. Cheng for collaboration and for their important contributions reviewed in this paper. This work was supported by the National Natural Science Foundation of China (Grant Nos. 11534001, 11822407, and 11674028), NBRPC (Grant Nos. 2017YFA0303301 and 2017YFA0304600), and NSF of Jiangsu Province, China (Grant No. BK20160007). H. Jiang was also funded by the Priority Academic Program Development of Jiangsu Higher Education Institutions.

References and notes

1. D. J. Thouless, M. Kohmoto, M. P. Nightingale, and M. den Nijs, Quantized Hall conductance in a two-dimensional periodic potential, *Phys. Rev. Lett.* 49(6), 405 (1982)
2. K. von Klitzing, G. Dorda, and M. Pepper, New method for high-accuracy determination of the fine-structure constant based on quantized Hall resistance, *Phys. Rev. Lett.* 45(6), 494 (1980)
3. K. von Klitzing, 25 years of quantum Hall effects: A personal view on the discovery, physics and applications of this quantum effect, *Séminaire Poincaré* 2, 1 (2004)
4. D. J. Thouless, M. Kohmoto, M. P. Nightingale, and M. den Nijs, Quantized Hall conductance in a two-dimensional periodic potential, *Phys. Rev. Lett.* 49(6), 405 (1982)
5. M. Kohmoto, Topological invariant and the quantization of the Hall conductance, *Ann. Phys.* 160(2), 343 (1985)
6. F. D. M. Haldane, Model for a quantum Hall effect without Landau levels: Condensed-matter realization of the "parity anomaly", *Phys. Rev. Lett.* 61(18), 2015 (1988)
7. C. Z. Chang, J. Zhang, X. Feng, J. Shen, Z. Zhang, M. Guo, K. Li, Y. Ou, P. Wei, L. L. Wang, Z. Q. Ji, Y. Feng, S. Ji, X. Chen, J. Jia, X. Dai, Z. Fang, S. C. Zhang, K. He, Y. Wang, L. Lu, X. C. Ma, and Q. K. Xue, Experimental observation of the quantum anomalous Hall effect in a magnetic topological insulator, *Science* 340(6129), 167 (2013)
8. C. L. Kane and E. J. Mele, Quantum spin Hall effect in graphene, *Phys. Rev. Lett.* 95(22), 226801 (2005)
9. C. L. Kane and E. J. Mele, Z_2 topological order and the quantum spin Hall effect, *Phys. Rev. Lett.* 95(14), 146802 (2005)
10. H. Min, J. E. Hill, N. A. Sinitsyn, B. R. Sahu, L. Kleinman, and A. H. MacDonald, Intrinsic and Rashba spin–orbit interactions in graphene sheets, *Phys. Rev. B* 74, 165310 (2006)

11. D. Huertas-Hernando, F. Guinea, and A. Brataas, Spin-orbit coupling in curved graphene, fullerenes, nanotubes, and nanotube caps, *Phys. Rev. B* 74(15), 155426 (2006)
12. Y. G. Yao, F. Ye, X.-L. Qi, S.-C. Zhang, and Z. Fang, Spin-orbit gap of graphene: First-principles calculations, *Phys. Rev. B* 75, 041401(R) (2007)
13. J. C. Boettger and S. B. Trickey, First-principles calculation of the spin–orbit splitting in graphene, *Phys. Rev. B* 75, 121402(R) (2007)
14. M. Gmitra, S. Konschuh, C. Ertler, C. Ambrosch-Draxl, and J. Fabian, Band-structure topologies of graphene: Spin–orbit coupling effects from first principles, *Phys. Rev. B* 80(23), 235431 (2009)
15. B. A. Bernevig and S. C. Zhang, Quantum spin Hall effect, *Phys. Rev. Lett.* 96(10), 106802 (2006)
16. B. A. Bernevig, T. L. Hughes, and S. C. Zhang, Quantum spin Hall effect and topological phase transition in HgTe quantum wells, *Science* 314(5806), 1757 (2006)
17. M. König, S. Wiedmann, C. Brune, A. Roth, H. Buhmann, L. W. Molenkamp, X. L. Qi, and S. C. Zhang, Quantum spin Hall insulator state in HgTe quantum wells, *Science* 318(5851), 766 (2007)
18. I. Knez, R. R. Du, and G. Sullivan, Evidence for helical edge modes in inverted InAs/GaSb quantum wells, *Phys. Rev. Lett.* 107(13), 136603 (2011)
19. S. Murakami, Quantum spin Hall effect and enhanced magnetic response by spin–orbit coupling, *Phys. Rev. Lett.* 97(23), 236805 (2006)
20. C. C. Liu, W. Feng, and Y. Yao, Quantum spin Hall effect in silicene and two-dimensional germanium, *Phys. Rev. Lett.* 107(7), 076802 (2011)
21. F. C. Chuang, L. Z. Yao, Z. Q. Huang, Y. T. Liu, C. H. Hsu, T. Das, H. Lin, and A. Bansil, Prediction of large-gap two-dimensional topological insulators consisting of bilayers of group III elements with Bi, *Nano Lett.* 14(5), 2505 (2014)
22. J. J. Zhou, W. Feng, C. C. Liu, S. Guan, and Y. Yao, Large-Gap Quantum Spin Hall insulator in single layer bismuth monobromide Bi_4Br_4, *Nano Lett.* 14(8), 4767 (2014)
23. W. Luo and H. J. Xiang, Room temperature quantum spin Hall insulators with a buckled square lattice, *Nano Lett.* 15(5), 3230 (2015)
24. Y. D. Ma, L. Kou, A. Du, and T. Heine, Group 14 element-based noncentrosymmetric quantum spin Hall insulators with large bulk gap, *Nano Res.* 8(10), 3412 (2015)
25. C. Si, J. Liu, Y. Xu, J. Wu, B.L. Gu, and W. Duan, Functionalized germanene as a prototype of large-gap two-dimensional topological insulators, *Phys. Rev. B* 89(11), 115429 (2014)
26. Y. Xu, B. Yan, H. J. Zhang, J. Wang, G. Xu, P. Tang, W. Duan, and S. C. Zhang, Large-gap quantum spin Hall insulators in tin films, *Phys. Rev. Lett.* 111(13), 136804 (2013)
27. Y. D. Ma, Y. Dai, L. Kou, T. Frauenheim, and T. Heine, Robust two-dimensional topological insulators in methyl-functionalized bismuth, antimony, and lead bilayer films, *Nano Lett.* 15(2), 1083 (2015)
28. Z. G. Song, C. C. Liu, J. Yang, J. Han, M. Ye, B. Fu, Y. Yang, Q. Niu, J. Lu, and Y. Yao, Quantum spin Hall insulators and quantum valley Hall insulators of BiX/SbX (X = H, F, Cl and Br) monolayers with a record bulk band gap, *NPG Asia Mater.* 6(12), e147 (2014)
29. H. M. Weng, X. Dai, and Z. Fang, Transition-metal pentatelluride $ZrTe_5$ and $HfTe_5$: A paradigm for large-gap quantum spin Hall insulators, *Phys. Rev. X* 4(1), 011002 (2014)
30. Y. D. Ma, L. Kou, X. Li, Y. Dai, S. C. Smith, and T. Heine, Quantum spin Hall effect and topological phase transition in two-dimensional square transition-metal dichalcogenides, *Phys. Rev. B* 92(8), 085427 (2015)
31. Y. D. Ma, L. Kou, X. Li, Y. Dai, and T. Heine, Two-dimensional transition metal dichalcogenides with a hexagonal lattice: Room-temperature quantum spin Hall insulators, *Phys. Rev. B* 93(3), 035442 (2016)
32. S. M. Nie, Z. Song, H. Weng, and Z. Fang, Quantum spin Hall effect in two-dimensional transition-metal dichalcogenide haeckelites, *Phys. Rev. B* 91(23), 235434 (2015)
33. X. F. Qian, J. Liu, L. Fu, and J. Li, Quantum spin Hall effect in two-dimensional transition metal dichalcogenides, *Science* 346(6215), 1344 (2014)
34. Y. D. Ma, L. Kou, X. Li, Y. Dai, and T. Heine, Room temperature quantum spin Hall states in two-dimensional crystals composed of pentagonal rings and their quantum wells, *NPG Asia Mater.* 8(4), e264 (2016)
35. Z. F. Wang, N. Su, and F. Liu, Prediction of a two-dimensional organic topological insulator, *Nano Lett.* 13(6), 2842 (2013)
36. B. Zhao, J. Zhang, W. Feng, Y. Yao, and Z. Yang, Quantum spin Hall and Z_2 metallic states in an organic material, *Phys. Rev. B* 90(20), 201403 (2014)
37. E. M. Spanton, K. C. Nowack, L. J. Du, G. Sullivan, R. R. Du, and K. A. Moler, Images of edge current in InAs/GaSb quantum wells, *Phys. Rev. Lett.* 113(2), 026804 (2014)
38. L. J. Du, I. Knez, G. Sullivan, and R. R. Du, Robust helical edge transport in gated InAs/GaSb bilayers, *Phys. Rev. Lett.* 114(9), 096802 (2015)
39. S. F. Wu, V. Fatemi, Q. D. Gibson, K. Watanabe, T. Taniguchi, R. J. Cava, and P. Jarillo-Herrero, Observation of the quantum spin Hall efft up to 100 kelvin in a monolayer crystal, *Science* 359(6371), 76 (2018)
40. F. Reis, G. Li, L. Dudy, M. Bauernfeind, S. Glass, W. Hanke, R. Thomale, J. Schafer, and R. Claessen, Bismuthene on a SiC substrate: A candidate for a high-temperature quantum spin Hall material, *Science* 357(6348), 287 (2017)
41. Z. Y. Fei, T. Palomaki, S. Wu, W. Zhao, X. Cai, B. Sun, P. Nguyen, J. Finney, X. Xu, and D. H. Cobden, Edge conduction in monolayer WTe_2, *Nat. Phys.* 13(7), 677 (2017)

42. S. J. Tang, C. Zhang, D. Wong, Z. Pedramrazi, H. Z. Tsai, C. Jia, B. Moritz, M. Claassen, H. Ryu, S. Kahn, J. Jiang, H. Yan, M. Hashimoto, D. Lu, R. G. Moore, C. C. Hwang, C. Hwang, Z. Hussain, Y. Chen, M. M. Ugeda, Z. Liu, X. Xie, T. P. Devereaux, M. F. Crommie, S. K. Mo, and Z. X. Shen, Quantum spin Hall state in monolayer 1T′-WTe_2, *Nat. Phys.* 13(7), 683 (2017)
43. A. Roth, C. Brne, H. Buhmann, L. W. Molenkamp, J. Maciejko, X. L. Qi, and S. C. Zhang, Nonlocal transport in the quantum spin Hall state, *Science* 325(5938), 294 (2009)
44. I. Knez, C. T. Rettner, S. H. Yang, S. S. P. Parkin, L. J. Du, R. R. Du, and G. Sullivan, Observation of edge transport in the disordered regime of topologically insulating InAs/GaSb quantum wells, *Phys. Rev. Lett.* 112(2), 026602 (2014)
45. J. J. Zhou, T. Zhou, S.-G. Cheng, H. Jiang, and Z. Q. Yang, Engineering topological quantum dot through planar magnetization in bismuthene, arxiv: 1812.11514 (2018)
46. L. Fu and C. L. Kane, Topological insulators with inversion symmetry, *Phys. Rev. B* 76(4), 045302 (2007)
47. D. Hsieh, D. Qian, L. Wray, Y. Xia, Y. S. Hor, R. J. Cava, and M. Z. Hasan, A topological Dirac insulator in a quantum spin Hall phase, *Nature* 452(7190), 970 (2008)
48. H. Zhang, C. X. Liu, X. L. Qi, X. Dai, Z. Fang, and S. C. Zhang, Topological insulators in Bi_2Se_3, Bi_2Te_3 and Sb_2Te_3 with a single Dirac cone on the surface, *Nat. Phys.* 5(6), 438 (2009)
49. Y. Xia, D. Qian, D. Hsieh, L. Wray, A. Pal, H. Lin, A. Bansil, D. Grauer, Y. S. Hor, R. J. Cava, and M. Z. Hasan, Observation of a large-gap topological-insulator class with a single Dirac cone on the surface, *Nat. Phys.* 5(6), 398 (2009)
50. D. Hsieh, Y. Xia, L. Wray, D. Qian, A. Pal, J. H. Dil, J. Osterwalder, F. Meier, G. Bihlmayer, C. L. Kane, Y. S. Hor, R. J. Cava, and M. Z. Hasan, Observation of unconventional quantum spin textures in topological insulators, *Science* 323(5916), 919 (2009)
51. Y. L. Chen, J. G. Analytis, J. H. Chu, Z. K. Liu, S.K. Mo, X. L. Qi, H. J. Zhang, D. H. Lu, X. Dai, Z. Fang, S. C. Zhang, I. R. Fisher, Z. Hussain, and Z. X. Shen, Experimental realization of a three-dimensional topological insulator Bi_2Te_3, *Science* 325(5937), 178 (2009)
52. J. S. Zhang, C. Z. Chang, Z. C. Zhang, J. Wen, X. Feng, K. Li, M. H. Liu, K. He, L. L. Wang, X. Chen, Q. K. Xue, X. C. Ma, and Y. Y. Wang, Band structure engineering in $(Bi_{1-x}Sb_x)_2Te_3$ ternary topological insulators, *Nat. Commun.* 2(1), 574 (2011)
53. D. Kim, S. Cho, N. P. Butch, P. Syers, K. Kirshenbaum, S. Adam, J. Paglione, and M. S. Fuhrer, Surface conduction of topological Dirac electrons in bulk insulating Bi Bi_2Se_3, *Nat. Phys.* 8(6), 459 (2012)
54. Y. Xu, I. Miotkowski, C. Liu, J. F. Tian, H. Nam, N. Alidoust, J. N. Hu, C. K. Shih, M. Z. Hasan, and Y. P. Chen, Observation of topological surface state quantum Hall effect in an intrinsic three-dimensional topological insulator, *Nat. Phys.* 10(12), 956 (2014)
55. D. A. Kozlov, Z. D. Kvon, E. B. Olshanetsky, N. N. Mikhailov, S. A. Dvoretsky, and D. Weiss, Transport properties of a 3D topological insulator based on a strained high-mobility HgTe film, *Phys. Rev. Lett.* 112(19), 196801 (2014)
56. J. Liao, Y. B. Ou, X. Feng, S. Yang, C. J. Lin, W. M. Yang, K. H. Wu, K. He, X. C. Ma, Q. K. Xue, and Y. Q. Li, Observation of Anderson localization in ultrathin films of three-dimensional topological insulators, *Phys. Rev. Lett.* 114(21), 216601 (2015)
57. H. C. Wang, H. W. Liu, C. Z. Chang, H. K. Zuo, Y. F. Zhao, Y. Sun, Z. C. Xia, K. He, X. C. Ma, X. C. Xie, Q. K. Xue, and J. Wang, Crossover between weak antilocalization and weak localization of bulk states in ultrathin Bi_2Se_3 films, *Sci. Rep.* 4(1), 5817 (2015)
58. D. Hsieh, Y. Xia, D. Qian, L. Wray, J. H. Dil, F. Meier, J. Osterwalder, L. Patthey, J. G. Checkelsky, N. P. Ong, A. V. Fedorov, H. Lin, A. Bansil, D. Grauer, Y. S. Hor, R. J. Cava, and M. Z. Hasan, A tunable topological insulator in the spin helical Dirac transport regime, *Nature* 460(7259), 1101 (2009)
59. L. Fu, Topological crystalline insulators, *Phys. Rev. Lett.* 106(10), 106802 (2011)
60. C. K. Chiu, J. C. Y. Teo, A. P. Schnyder, and S. Ryu, Classification of topological quantum matter with symmetries, *Rev. Mod. Phys.* 88(3), 035005 (2016)
61. S. Chakravarty and A. Schmid, Weak localization: The quasiclassical theory of electrons in a random potential, *Phys. Rep.* 140(4), 193 (1986)
62. A. Stern, Y. Aharonov, and Y. Imry, Phase uncertainty and loss of interference: A general picture, *Phys. Rev. A* 41(7), 3436 (1990)
63. H. Jiang, S. Cheng, Q. F. Sun, and X. C. Xie, Topological insulator: A new quantized spin Hall resistance robust to dephasing, *Phys. Rev. Lett.* 103(3), 036803 (2009)
64. I. Żutić, J. Fabian, and S. Das Sarma, Spintronics: Fundamentals and applications, *Rev. Mod. Phys.* 76(2), 323 (2004)
65. J. Fabian, A. Matos-Abiague, C. Ertler, P. Stano, and I. Zutic, Semiconductor spintronics, *Acta Phys. Slovaca* 57(4–5), 565 (2007)
66. T. L. Schmidt, S. Rachel, F. von Oppen, and L. I. Glazman, Inelastic electron backscattering in a generic helical edge channel, *Phys. Rev. Lett.* 108(15), 156402 (2012)
67. J. I. Väyrynen, M. Goldstein, and L. I. Glazman, Helical edge resistance introduced by charge puddles, *Phys. Rev. Lett.* 110(21), 216402 (2013)
68. J. C. Budich, F. Dolcini, P. Recher, and B. Trauzettel, Phonon-induced backscattering in helical edge states, *Phys. Rev. Lett.* 108(8), 086602 (2012)
69. J. J. Qi, H. W. Liu, H. Jiang, and X. C. Xie, Effective spin dephasing mechanism in confined two-dimensional topological insulators, *Sci. China Phys. Mech. Astron.* 59(7), 677811 (2016)
70. H. W. Liu, H. Jiang, Q. F. Sun, and X. C. Xie, Dephasing effect on backscattering of helical surface states in 3D topological insulators, *Phys. Rev. Lett.* 113(4), 046805 (2014)

71. J. Liao, Y. B. Ou, H. W. Liu, K. He, X. C. Ma, Q. K. Xue, and Y. Q. Li, Enhanced electron dephasing in three-dimensional topological insulators, *Nat. Commun.* 8(1), 16071 (2017)
72. C. Wu, B. A. Bernevig, and S. C. Zhang, Helical liquid and the edge of quantum spin Hall systems, *Phys. Rev. Lett.* 96(10), 106401 (2006)
73. Q. F. Sun, J. Wang, and H. Guo, Quantum transport theory for nanostructures with Rashba spin–orbital interaction, *Phys. Rev. B* 71(16), 165310 (2005)
74. Y. Meir and N. S. Wingreen, Landauer formula for the current through an interacting electron region, *Phys. Rev. Lett.* 68(16), 2512 (1992)
75. A. P. Jauho, N. S. Wingreen, and Y. Meir, Time-dependent transport in interacting and noninteracting resonant-tunneling systems, *Phys. Rev. B* 50(8), 5528 (1994)
76. S. Datta, Electronic Transport in Mesoscopic Systems, Cambridge: Cambridge University Press, 1995
77. M. Büttiker, Role of quantum coherence in series resistors, *Phys. Rev. B* 33(5), 3020 (1986)
78. Y. X. Xing, Q. F. Sun, and J. Wang, Inuence of dephasing on the quantum Hall effect and the spin Hall effect, *Phys. Rev. B* 77(11), 115346 (2008)
79. E. J. Koop, B. J. van Wees, D. Reuter, A. D. Wieck, and C. H. van der Wal, Spin accumulation and spin relaxation in a large open quantum dot, *Phys. Rev. Lett.* 101(5), 056602 (2008)
80. S. M. Frolov, A. Venkatesan, W. Yu, J. A. Folk, and W. Wegscheider, Electrical generation of pure spin currents in a two-dimensional electron gas, *Phys. Rev. Lett.* 102(11), 116802 (2009)
81. Q. F. Sun, Y. X. Xing, and S. Q. Shen, Double quantum dot as detector of spin bias, *Phys. Rev. B* 77(19), 195313 (2008)
82. Y. X. Xing, Q. F. Sun, and J. Wang, Spin bias measurement based on a quantum point contact, *Appl. Phys. Lett.* 93(14), 142107 (2008)
83. Y. K. Kato, R. C. Myers, A. C. Gossard, and D. D. Awschalom, Observation of the spin Hall effect in Semiconductors, *Science* 306(5703), 1910 (2004)
84. V. Sih, W. H. Lau, R. C. Myers, V. R. Horowitz, A. C. Gossard, and D. D. Awschalom, Generating spin currents in semiconductors with the spin Hall effect, *Phys. Rev. Lett.* 97(9), 096605 (2006)
85. M. König, M. Baenninger, A. G. F. Garcia, N. Harjee, B. L. Pruitt, C. Ames, P. Leubner, C. Brüne, H. Buhmann, L. W. Molenkamp, and D. Goldhaber-Gordon, Spatially resolved study of backscattering in the quantum spin Hall state, *Phys. Rev. X* 3, 021003 (2013)
86. R. Jackiw and C. Rebbi, Solitons with fermion number 1/2, *Phys. Rev. D* 13(12), 3398 (1976)
87. F. Zhang, C. L. Kane, and E. J. Mele, Surface states of topological insulators, *Phys. Rev. B* 86(8), 081303 (2012)
88. W. Y. Shan, J. Lu, H. Z. Lu, and S. Q. Shen, Vacancy-induced bound states in topological insulators, *Phys. Rev. B* 84(3), 035307 (2011)
89. A. Ström, H. Johannesson, and G. I. Japaridze, Edge dynamics in a quantum spin Hall state: Effects from Rashba spin–orbit interaction, *Phys. Rev. Lett.* 104(25), 256804 (2010)
90. J. Fabian and S. Das Sarma, Phonon-induced spin relaxation of conduction electrons in aluminum, *Phys. Rev. Lett.* 83(6), 1211 (1999)
91. G. Grimvall, Electron–Phonon Interaction in Metals, North-Holland Pub, 1981
92. K. Saha and I. Garate, Phonon-induced topological insulation, *Phys. Rev. B* 89(20), 205103 (2014)
93. E. Lhuillier, S. Keuleyan, and P. Guyot-Sionnest, Optical properties of HgTe colloidal quantum dots, *Nanotechnology* 23(17), 175705 (2012)
94. A. Fasolino, E. Molinari, and J. C. Maan, Calculated superlattice and interface phonons of InAs/GaSb superlattices, *Phys. Rev. B* 33(12), 8889 (1986)
95. D. Hernangómez-Pérez, J. Ulrich, S. Florens, and T. Champel, Spectral properties and local density of states of disordered quantum Hall systems with Rashba spin–orbit coupling, *Phys. Rev. B* 88(24), 245433 (2013)
96. S. Y. Xu, Y. Xia, L. A. Wray, S. Jia, F. Meier, J. H. Dil, J. Osterwalder, B. Slomski, A. Bansil, H. Lin, R. J. Cava, and M. Z. Hasan, Topological phase transition and texture inversion in a tunable topological insulator, *Science* 332(6029), 560 (2011)
97. T. Sato, K. Segawa, K. Kosaka, S. Souma, K. Nakayama, K. Eto, T. Minami, Y. Ando, and T. Takahashi, Unexpected mass acquisition of Dirac fermions at the quantum phase transition of a topological insulator, *Nat. Phys.* 7(11), 840 (2011)
98. S. Y. Xu, M. Neupane, C. Liu, D. M. Zhang, A. Richardella, L. A. Wray, N. Alidoust, M. Leandersson, T. Balasubramanian, J. Snchez-Barriga, O. Rader, G. Landolt, B. Slomski, J. H. Dil, J. Osterwalder, T. R. Chang, H. T. Jeng, H. Lin, A. Bansil, N. Samarth, and M. Z. Hasan, Hedgehog spin texture and Berrys phase tuning in a magnetic topological insulator, *Nat. Phys.* 8(8), 616 (2012)
99. S. Souma, M. Komatsu, M. Nomura, T. Sato, A. Takayama, T. Takahashi, K. Eto, K. Segawa, and Y. Ando, Spin polarization of gapped Dirac surface states near the topological phase transition in $TlBi(S_{1-x}Se_x)_2$, *Phys. Rev. Lett.* 109(18), 186804 (2012)
100. B. L. Altshuler and A. G. Aronov, Electron–Electron Interactions in Disordered Systems, edited by A. L. Efros and M. Pollak, Elsevier, Amsterdam, 1985
101. D. Belitz and S. Das Sarma, Inelastic phase-coherence time in thin metal films, *Phys. Rev. B* 36(14), 7701 (1987)
102. V. B. Berestetskii, E. M. Lifshits, and L. P. Pitaevskii, Quantum Electrodynamics, Elsevier, Oxford, 1971
103. Y. Imry, Introduction to Mesoscopic Physics, Oxford University Press, 2008
104. B. L. Altshuler, A. G. Aronov, and D. E. Khmelnitsky, Effects of electron–electron collisions with small energy transfers on quantum localisation, *J. Phys. C Solid State Phys.* 15(36), 7367 (1982)

105. B. I. Shklovskii and A. L. Efros, Electron Properties of Doped Semiconductors, Springer Science and Business Media, 2013

106. S. Malzard, C. Poli, and H. Schomerus, Topologically protected defect states in open photonic systems with non-Hermitian charge-conjugation and parity-time symmetry, *Phys. Rev. Lett.* 115(20), 200402 (2015)

107. P. San-Jose, J. Cayao, E. Prada, and R. Aguado, Majorana bound states from exceptional points in non-topological superconductors, *Sci. Rep.* 6(1), 21427 (2016)

108. T. E. Lee, Anomalous edge state in a non-Hermitian lattice, *Phys. Rev. Lett.* 116(13), 133903 (2016)

109. D. Leykam, K. Y. Bliokh, C. Huang, Y. D. Chong, and F. Nori, Edge modes, degeneracies, and topological numbers in non-Hermitian systems, *Phys. Rev. Lett.* 118(4), 040401 (2017)

110. Y. Xu, S. T. Wang, and L. M. Duan, Weyl exceptional rings in a three-dimensional dissipative cold atomic gas, *Phys. Rev. Lett.* 118(4), 045701 (2017)

111. Z. P. Gong, Y. Ashida, K. Kawabata, K. Takasan, S. Higashikawa, and M. Ueda, Topological phases of non-Hermitian systems, *Phys. Rev. X* 8(3), 031079 (2018)

112. H. Jiang, C. Yang, and S. Chen, Topological invariants and phase diagrams for one-dimensional two-band non-Hermitian systems without chiral symmetry, *Phys. Rev. A* 98(5), 052116 (2018)

113. S. Y. Yao and Z. Wang, Edge states and topological invariants of non-Hermitian systems, *Phys. Rev. Lett.* 121(8), 086803 (2018)

114. S. Y. Yao, F. Song, and Z. Wang, Non-Hermitian Chern bands, *Phys. Rev. Lett.* 121(13), 136802 (2018)

115. Private communication with Y. Y. Wang.

116. F. Evers and A. D. Mirlin, Anderson transitions, *Rev. Mod. Phys.* 80(4), 1355 (2008)

117. J. J. Qi, H. W. Liu, C. Z. Chen, H. Jiang, and X. C. Xie, Quantum to classical crossover under dephasing effects in a two-dimensional percolation model, arxiv: 1903.01764 (2019)

118. H. Jiang, L. Wang, Q. F. Sun, and X. C. Xie, Numerical study of the topological Anderson insulator in HgTe/CdTe quantum wells, *Phys. Rev. B* 80(16), 165316 (2009)

119. D. W. Xu, J. J. Qi, J. Liu, X. C. Sacksteder, X. C. Xie, and H. Jiang, Phase structure of the topological Anderson insulator, *Phys. Rev. B* 85(19), 195140 (2012)

120. C. Z. Chen, H. W. Liu, H. Jiang, Q. F. Sun, Z. Q. Wang, and X. C. Xie, Tunable Anderson metal-insulator transition in quantum spin-Hall insulators, *Phys. Rev. B* 91(21), 214202 (2015)

121. C. Z. Chen, J. T. Song, H. Jiang, Q. F. Sun, Z. Q. Wang, and X. C. Xie, Disorder and metal-insulator transitions in Weyl semimetals, *Phys. Rev. Lett.* 115(24), 246603 (2015)

122. C. Z. Chen, H. Liu, and X. C. Xie, Effects of random domains on the zero Hall plateau in the quantum anomalous Hall effect, *Phys. Rev. Lett.* 122(2), 026601 (2019)

123. Y. Ando and L. Fu, Topological crystalline insulators and topological superconductors: From concepts to materials, *Annu. Rev. Condens. Matter Phys.* 6(1), 361 (2015)

124. B. H. Yan and C. Felser, Topological materials: Weyl semimetals, *Annu. Rev. Condens. Matter Phys.* 8(1), 337 (2017)

125. W. A. Benalcazar, B. A. Bernevig, and T. L. Hughes, Quantized electric multipole insulators, *Science* 357(6346), 61 (2017)